Trichromatic shaper-based quantum state holography

K. Eickhoff , L. Feld, D. Köhnke , T. Bayer, and M. Wollenhaupt *

Institut für Physik, Carl von Ossietzky Universität Oldenburg, Carl-von-Ossietzky-Straße 9-11, D-26129 Oldenburg, Germany

We present an ultrafast quantum state holography scheme based on the interference of photoelectron wave packets from multiphoton ionization (MPI) using shaper-generated trichromatic pulse sequences. By superimposing a probe and a reference electron wave packet generated by MPI with a pump-probe-reference triple-pulse sequence, the phases from the MPI dynamics are imprinted into the resulting photoelectron hologram. In the experiment, we combine white-light supercontinuum pulse shaping with differential photoelectron detection using a velocity-map-imaging spectrometer. To illustrate the holographic scheme, we study the interference of a probe wave packet from (2+1) resonance-enhanced MPI of potassium atoms via the 3*d* state with a reference wave packet from nonresonant three-photon MPI of its 4*s* ground state. Phase control of the hologram is exerted by variation of the relative phases of the individual pulses in the sequence. We analyze the hologram to determine the time- and energy-dependent quantum phases resulting from either the free time evolution of the probe wave packet or the detuning of the pump pulse with respect to the resonance and the ensuing time evolution in the excited state of the atom. Our results show that the trichromatic shaper-based photoelectron holography scheme is a powerful tool for time-resolved and phase-sensitive background-free observation of ultrafast quantum dynamics.

I. INTRODUCTION

The wave function of a quantum-mechanical system, such as an electron, atom, or a molecule, is characterized completely by its modulus and its phase. In general, only the probability density, i.e., the modulus square, is directly observable [1,2]. However, knowledge of the phase is vital to determine other observables, e.g., the momentum distribution [3–6] and the probability current density [7–10], and to make predictions on the time evolution of the system. In addition, detailed information about the system's past is also encoded in the phase, enabling us to draw conclusions on the underlying physical mechanisms. Dynamical processes are generally described by nonstationary wave functions, i.e., wave packets, which are usually expanded into energy eigenstates. The relative phases between these states then determine the time evolution of the system and encode dynamical information. Measurement of the phase, in general, offers deeper insights into the origin and history of the wave function.

Advanced experimental techniques have been devised to retrieve quantum-mechanical phase information and determine the wave function [11–15]. Recent applications range from the reconstruction of vibrational wave packets in molecules [16,17] and the design and characterization of Rydberg wave packets in atoms [11,18–21] to the phase-sensitive detection and analysis of free-electron wave packets from multiphoton [14,22] and tunneling ionization [13,23,24]. Especially, the principles of strong-field photoelectron holography were recently reviewed in [6]. The common ground

in these experiments is the use of holographic methods, introduced in optics by Gábor [25,26] and later transferred to quantum mechanics by Leichtle *et al.* [27,28], who coined the term *quantum state holography*. Briefly, quantum state holography is based on the interference of a probe state with a well-characterized reference state. The probe state maps the object or target state of interest, whereas the reference state is excited directly. Suitable detection of the resulting interference pattern enables the reconstruction of the target-state wave function.

Recently, we developed a pulse-shaper-based technique for time-resolved holographic imaging of ultrafast electron dynamics [21]. Shaper-based quantum state holography (SQuaSH) builds on the bichromatic pump-probe scheme introduced in [29,30], using the pump pulse to initiate a dynamical process and the probe pulse to *simultaneously* map the dynamics into the ionization continuum and provide a reference by direct ground-state ionization. With a suitable design of commensurable central frequencies $N_{pu}\omega_{pu} = N_{pr}\omega_{pr}$, where N_{pu} is the number of pump photons used for the resonant excitation and N_{pr} is the number of probe photons adding up to the same energy, the created probe and reference photoelectron wave packet interfere to form a photoelectron hologram. Due to the bichromatic approach, the holographic signal is disentangled energetically from the single-color background. Measurement of the three-dimensional (3D) photoelectron momentum distribution (PMD) of the hologram, e.g., using photoelectron tomography [31], hence enables the phase-sensitive and background-free reconstruction of the dynamics.

Here, we present a further development of the self-referenced holographic scheme discussed in [21] by adding

---

*Matthias.Wollenhaupt@uol.de

an independent reference pulse with a third color. Hence, the new scheme is referred to as trichromatic SQuaSH. By decoupling the probe from the reference step, the above condition linking the frequencies of the pump and probe pulses is lifted. This approach allows us to tailor the probe pulse to the application at hand. The reference frequency ω_{ref} is adapted to the pump and probe frequencies by the generalized condition $N_{\text{pu}}\omega_{\text{pu}} + N_{\text{pr}}\omega_{\text{pr}} = N_{\text{ref}}\omega_{\text{ref}}$. Here, N_{pr} and N_{ref} are the numbers of probe and reference photons used for ionization from the excited state and ground state, respectively. We note that if the photon numbers satisfy the additional condition $N_{\text{pu}} + N_{\text{pr}} = N_{\text{ref}}$, i.e., both ionization pathways are of the same order, trichromatic SQuaSH is insensitive to the carrier-envelope phase (CEP) of the laser field [32].

The trichromatic SQuaSH scheme is demonstrated in a proof-of-concept experiment on the (2+1) resonance-enhanced multiphoton ionization (REMPI) of potassium atoms via the $3d$ state. The trichromatic pump-probe-reference pulse sequences are generated by white-light polarization pulse shaping [33]. The pump pulse is tuned to the two-photon resonance $4s \rightarrow\rightarrow 3d$, while probe and reference pulses are designed such that the probe photoelectron wave packet from one-photon ionization of the $3d$ state overlaps with the reference wave packet from three-photon ionization of the $4s$ ground state. The resulting photoelectron hologram is measured using velocity-map-imaging (VMI) spectroscopy [3].

In the first part of the experiment, we demonstrate optical phase control of the photoelectron hologram. By systematically varying the relative phase of each of the three pulses, we record energy-resolved interference patterns. The interference patterns exhibit a characteristic periodical phase dependency reflecting the orders of the underlying multiphoton ionization (MPI) processes. In the second part, we apply the trichromatic SQuaSH technique to study quantum-dynamical phases imprinted in the hologram by the ionization dynamics. While the bound-state time evolution results in an overall phase shift of the phase-resolved interference pattern, the time evolution in the continuum manifests in a shearing of the interference fringes. Our studies show that the structure of the interference pattern reveals detailed information on the ionization dynamics. In general, the trichromatic shaper-based approach with fully tunable phases, time delays, and wavelengths of the spectral bands provides unprecedented options for multidimensional spectroscopy and coherent control.

II. PHYSICAL SYSTEM AND THEORETICAL MODEL

We investigate the MPI of K atoms using phase-locked trichromatic femtosecond laser pulse sequences. Here, we introduce the physical system and provide a theoretical description of the photoelectron wave packets measured in the experiment. The theoretical model is used for the analysis and discussion of the experimental results. We motivate the observables and derive analytical expressions to describe the experimental data (see also Appendix A).

The excitation scheme of K interacting perturbatively with a parallel linearly polarized (PLP) trichromatic pulse sequence is depicted in Fig. 1(a). The first pulse (red), centered around $\omega_{\text{pu}} = 2.03$ rad/fs and denoted as pump, excites the
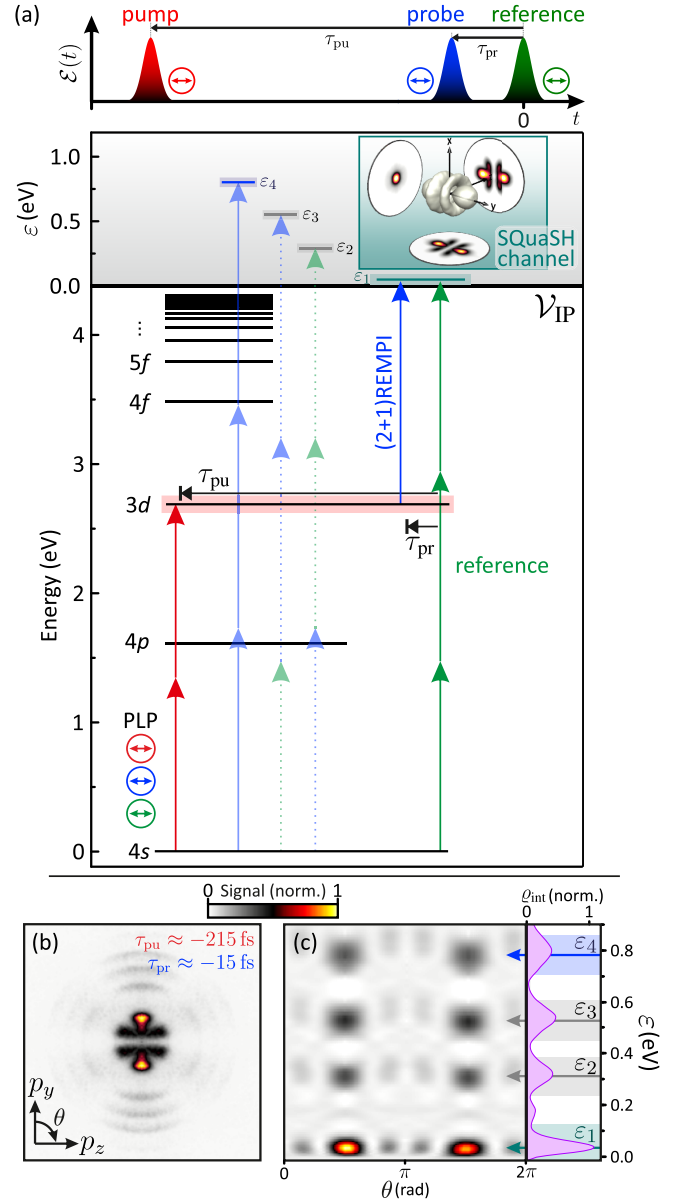

FIG. 1. (a) Excitation scheme of K atoms interacting perturbatively with a PLP pump-probe-reference pulse sequence. The pump pulse (red) launches a d-type wave packet by two-photon excitation. The time-delayed probe pulse (blue) maps the $3d$ population into an f-type photoelectron wave packet. This wave packet is holographically superimposed with an f-type reference wave packet originating from direct three-photon ionization of the $4s$ ground state with the reference pulse (green). The inset shows a measured and tomographically reconstructed 3D PMD of the resulting wave packet for a PLP pulse sequence. (b) and (c) show the measured 2D projection of the PMD for $\tau_{\text{pu}} \approx -215$ fs and $\tau_{\text{pr}} \approx -15$ fs in Cartesian and polar representations, where the addressed energy windows around ε_1 to ε_4 are highlighted.

$3d$ state by two-photon absorption ($N_{\text{pu}} = 2$). After a variable time delay, the second pulse (blue), centered around $\omega_{\text{pr}} = 2.61$ rad/fs and denoted as probe, maps the excited state into an f-type continuum by one-photon ionization ($N_{\text{pr}} = 1$). This time-delayed (2+1) REMPI process creates a probe photoelectron wave packet. For the holographic imaging of the

bound-state excitation dynamics, the probe wave packet is superimposed by a reference wave packet, created by nonresonant three-photon ionization ($N_{\text{ref}} = 3$) of the $4s$ ground state using a third pulse (green) centered around $\omega_{\text{ref}} = 2.22$ rad/fs and termed the reference pulse. The interference of probe and reference wave packets yields an $f(m = 0)$-type photoelectron hologram in a kinetic-energy window around

$$\varepsilon_1 = N_{\text{pu}}\hbar\omega_{\text{pu}} + N_{\text{pr}}\hbar\omega_{\text{pr}} - \mathcal{V}_{\text{IP}} = N_{\text{ref}}\hbar\omega_{\text{ref}} - \mathcal{V}_{\text{IP}} \approx 0.05 \text{ eV}, \tag{1}$$

which we refer to as the *SQuaSH channel* in the following. Here, $\mathcal{V}_{\text{IP}} = \hbar\omega_{\text{IP}}$ denotes the ionization potential. Note that for detuned excitation as discussed in Sec. IV B 2, $N_{\text{pu}}\hbar\omega_{\text{pu}}$ is replaced by $\hbar\omega_{3d}$ in Eq. (1) to preserve the overlap of the probe and reference wave packets. A measured two-dimensional (2D) projection of the PMD is depicted in Figs. 1(b) and 1(c) in Cartesian and polar representation, respectively. As shown in Appendix A, the hologram is sensitive to the relative phases between the three pulses since the (2+1) REMPI and direct three-photon ionization pathways are composed of different numbers of photons from each color. Although different colors are involved, both pathways are of the same order, $N_{\text{pu}} + N_{\text{pr}} = N_{\text{ref}} = 3$, so that the CEP accumulated in each pathway is the same, rendering the hologram insensitive to the CEP [32,34]. Following the nomenclature introduced in [32], we denote this interference the *mixed intraband interference*.

Besides the photoelectron hologram in the SQuaSH channel (highlighted in petrol blue at energy ε_1), additional contributions are observed at larger kinetic energies if the probe and reference pulses overlap in time. These contributions are attributed to frequency mixing [35] of the probe and reference pulses, creating photoelectron wave packets centered around $\varepsilon_2 = \hbar\omega_{\text{pr}} + 2\hbar\omega_{\text{ref}} - \mathcal{V}_{\text{IP}} \approx 0.30$ eV and $\varepsilon_3 = 2\hbar\omega_{\text{pr}} + \hbar\omega_{\text{ref}} - \mathcal{V}_{\text{IP}} \approx 0.56$ eV (both highlighted in gray). Finally, the single-color contribution of the probe pulse from direct three-photon ground-state ionization is observed, separated from the SQuaSH channel, around $\varepsilon_4 = 3\hbar\omega_{\text{pr}} - \mathcal{V}_{\text{IP}} \approx 0.81$ eV (highlighted in blue), allowing for background-free measurements.

In the PLP case, the trichromatic pulse sequence is completely described by the scalar electric fields of the three colors. The negative-frequency spectrum [36] of the total laser electric field is given by

$$\tilde{E}^-(\omega) = \sum_i \tilde{E}_i^-(\omega) = \sum_i \tilde{\mathcal{E}}_i(\omega + \omega_i)e^{i\Phi_i(\omega)}, \tag{2}$$

where $i \in \{\text{pu, pr, ref}\}$ indicates the respective spectral component. The functions $\tilde{\mathcal{E}}_i(\omega)$ are the spectral envelopes centered around the corresponding frequencies ω_i. In the experiment, the spectral phase functions $\Phi_i(\omega) = \varphi_i - (\omega + \omega_i)\tau_i$, with the constant relative phases φ_i and the individual time delays τ_i, are introduced by the pulse shaper. The common CEP is omitted because in the perturbative limit, it contributes only to the absolute phase of the photoelectron wave function (see Appendix A). The linear phases are applied relative to the central frequency of the respective spectral component (see the inset in Fig. 2). By this means, only the pulse envelopes are shifted in time by varying τ_i, while the carriers remain fixed [37–39], allowing us to disentangle the
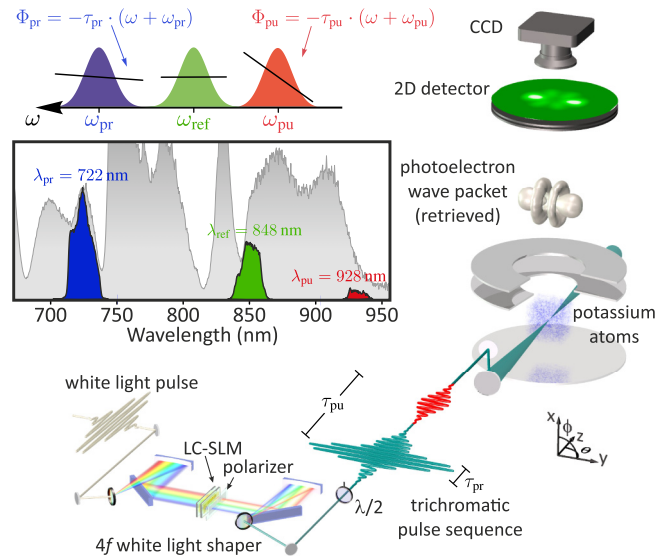

FIG. 2. Experimental setup for the shaper-based generation and manipulation of photoelectron holograms in trichromatic SQuaSH. The trichromatic pulse sequences are generated by amplitude and phase modulation of a WLS using a $4f$ polarization pulse shaper. The insets show the measured WLS (gray-shaded background) and the applied trichromatic amplitude profile together with a schematic representation of spectral amplitudes and phases. Photoelectron wave packets created by the interaction of K atoms with the trichromatic pulse sequence are imaged by a VMI spectrometer. Projections of the generated wave packets are measured by a position-sensitive 2D detector and recorded by a CCD camera.

variation of the time delay and relative phase between the pulses. In contrast, using an interferometer to shift a pulse in time locks the pulse envelope to the carrier such that the time delay is always accompanied by a constant phase offset. The inverse Fourier transformation of Eq. (2) yields the laser field in the time domain,

$$E^-(t) = \sum_i E_i^-(t) = \sum_i \mathcal{E}_i(t - \tau_i)e^{-i(\omega_i t - \varphi_i)}. \tag{3}$$

In the following, we choose $\tau_{\text{ref}} = 0$ fs as the time zero, implying that the pump and probe pulses are advanced in time, i.e., $\tau_{\text{pu}} < 0$ fs and $\tau_{\text{pr}} < 0$ fs.

Next, we consider the MPI of K with the field defined in Eq. (3), focusing on the photoelectron hologram in the SQuaSH channel. The wave function of the hologram in the momentum representation, with photoelectron momentum $\boldsymbol{k} = (k, \theta, \phi)$, is described by a superposition of the probe and the reference wave packet [21],

$$\Psi(\boldsymbol{k}) \propto (a_{\text{ref}}(k) + a_{\text{pr}}(k))\psi_{3,0}(\theta, \phi). \tag{4}$$

The corresponding amplitudes $a_{\text{ref}}(k)$ and $a_{\text{pr}}(k)$ determine the radial part and hence the kinetic-energy distribution of the photoelectron hologram. They are calculated using third-order time-dependent perturbation theory (see Appendix A for details). The angular distribution $\psi_{3,0}(\theta, \phi)$ is determined by the spherical harmonic $Y_{3,0}(\theta)$. Since $Y_{3,0}(\theta)$ is independent of the azimuthal angle ϕ, the wave function—in the PLP case—is cylindrically symmetric with respect to the y axis (polarization direction). The PMD measured in the experiment is described

by the photoelectron density $\varrho(\mathbf{k}) = |\Psi(\mathbf{k})|^2$, yielding an expression of the form

$$\varrho(\mathbf{k}) \propto [B(k) + S(k)\cos(\alpha_{\mathrm{opt}} + \beta(k) + \gamma_{\mathrm{qm}})]|\psi_{3,0}(\theta)|^2. \tag{5}$$

The first term in the square brackets corresponds to a background created by the probe and reference pulses independently. The second term describes the interference of the probe and reference wave packets. Since both ionization pathways lead to the same $f(m = 0)$-type continuum, implying the same angular distribution of both wave packets, the interference is observed along only the radial coordinate, i.e., in the energy-resolved photoelectron spectrum. The interference term is modulated by a cosine function with three phase contributions. The first contribution

$$\alpha_{\mathrm{opt}} = 3\varphi_{\mathrm{ref}} - (2\varphi_{\mathrm{pu}} + \varphi_{\mathrm{pr}}) \tag{6}$$

is fully determined by the optical field, i.e., contains the relative optical phases weighted by the number of photons involved in the corresponding ionization processes ($N_{\mathrm{pr}} = 1$, $N_{\mathrm{pu}} = 2$, $N_{\mathrm{ref}} = 3$). It describes the difference between the optical phases accumulated along the (2+1) REMPI and the nonresonant three-photon ionization pathway. The second contribution is given by

$$\beta(k) = \varpi_{\mathrm{pu}}\tau_{\mathrm{pu}} + \varpi_{\mathrm{holo}}(k)\tau_{\mathrm{pr}} \equiv \beta_{\mathrm{b}} + \beta_{\mathrm{f}}(k), \tag{7}$$

with the detunings $\varpi_{\mathrm{pu}} = 2\omega_{\mathrm{pu}} - \omega_{3d}$ and $\varpi_{\mathrm{holo}}(k) = 3\omega_{\mathrm{ref}} - \omega_{\mathrm{IP}} - \omega_k \equiv \omega_{\mathrm{pr}} + \omega_{3d} - \omega_{\mathrm{IP}} - \omega_k$ (see Appendix A for details). Equation (7) describes both the bound time evolution of the excited atom, with the term $\beta_{\mathrm{b}} = \varpi_{\mathrm{pu}}\tau_{\mathrm{pu}}$, and the free time evolution of the probe wave packet, with the energy-dependent phase term $\beta_{\mathrm{f}}(k) = \varpi_{\mathrm{holo}}(k)\tau_{\mathrm{pr}}$. Varying the detuning ϖ_{pu} of the pump pulse induces a constant phase shift β_{b} of the interference pattern due to the time evolution of the excited $3d$ state in the bound system. A probe pulse time delay induces a k-dependent phase $\beta_{\mathrm{f}}(k)$, reflecting the free time evolution of the probe wave packet in the continuum before it interferes with the reference wave packet [40]. This radial phase shifts the interference fringes differently for each continuum state $\varepsilon(k) = \hbar\omega_k = \frac{(\hbar k)^2}{2m_e}$, resulting in a tilt or shearing of the energy-resolved interference pattern (see Sec. IV B). To investigate this effect experimentally, we separated the probe from the reference pulse by $\tau_{\mathrm{pr}} \approx -15\,\mathrm{fs}$ in all measurements. The third phase contribution in Eq. (5), $\gamma_{\mathrm{qm}} = \chi_{\mathrm{ref}} - \chi_{\mathrm{pr}}$, describes the difference between the multiphoton ionization phases acquired along each pathway due to, e.g., the energy-level structure of the atom [41] (see Appendix A) or, in stronger laser fields, the dynamic Stark effect [42].

Because for PLP pulse sequences the phase information is encoded in the radial part of the photoelectron hologram, it is sufficient to analyze the kinetic-energy distribution of the measured projected PMDs. For a quantitative analysis of the experimental data, we apply the Abel inversion to retrieve a 2D section $\varrho(k, \theta)$ through the PMD in the y-z plane (parallel to the detector plane). This section is integrated over the polar angle θ, yielding the momentum-resolved spectrum

$$\varrho_{\mathrm{int}}(k) = \int_0^{2\pi} \varrho(k, \theta)\,d\theta, \tag{8}$$

which is then energy calibrated [43] to obtain the kinetic-energy-resolved photoelectron spectrum $\varrho_{\mathrm{int}}(\varepsilon)$. In the experiment, we study coherent control of the hologram by measuring energy-resolved photoelectron spectra while varying the relative optical phases. For this purpose, we decompose the phase $\alpha_{\mathrm{opt}} = \alpha_{\mathrm{v}} + \alpha_0$ into the phase to be varied α_{v} (i.e. $-2\varphi_{\mathrm{pu}}$, $-\varphi_{\mathrm{pr}}$, or $3\varphi_{\mathrm{ref}}$) and the sum of the two remaining phase terms α_0. The recorded energy-resolved spectra $\varrho_{\mathrm{int}}(\varepsilon, \alpha_{\mathrm{v}}; \alpha_0)$ plotted as a function of the variable phase α_{v} display an interference pattern in the SQuaSH channel ($\varepsilon_1 \approx 0.05\,\mathrm{eV}$), which we refer to as a phase map. The phase map is manipulated parametrically by the constant phase α_0. In particular, Eq. (5) shows that switching α_0 from 0 to π leads to an inversion of the phase map. This inversion is utilized to separate the interference term in Eq. (5) from the phase-insensitive background. Specifically, we perform two measurements of $\varrho_{\mathrm{int}}(\varepsilon, \alpha_{\mathrm{v}}; \alpha_0)$ for $\alpha_0 = 0$ and π and calculate the energy-resolved phase contrast

$$\mathcal{C}(\varepsilon, \alpha_{\mathrm{v}}) = \frac{\varrho_{\mathrm{int}}(\varepsilon, \alpha_{\mathrm{v}}; 0) - \varrho_{\mathrm{int}}(\varepsilon, \alpha_{\mathrm{v}}; \pi)}{\max[\varrho_{\mathrm{int}}(\varepsilon, \alpha_{\mathrm{v}}; 0) + \varrho_{\mathrm{int}}(\varepsilon, \alpha_{\mathrm{v}}; \pi)]}$$
$$\propto \cos(\alpha_{\mathrm{v}} + \beta(\varepsilon) + \gamma_{\mathrm{qm}}). \tag{9}$$

The phase contrast $\mathcal{C}(\varepsilon, \alpha_{\mathrm{v}})$ reveals the interference pattern without distortion by the energy-dependent background, which facilitates the retrieval of the energy-dependent phases imprinted in the hologram.

The theoretical model described by Eqs. (5)–(7) is employed in Sec. IV to obtain analytical expressions for physical quantities, e.g., the periodicity of the recorded phase maps (Sec. IV A), the tilt or shearing of the interference fringes due to the time-delayed creation of the reference wave packet (Sec. IV B 1), and the overall phase shift of the interference pattern due to the detuned excitation of the $3d$ state (Sec. IV B 2). These analytical expressions are compared with the experimental results.

III. EXPERIMENT

A. Experimental setup

In our experiment, we combine trichromatic white-light polarization pulse shaping with photoelectron imaging [3]. Infrared pulses provided by a multipass chirped-pulse amplifier (Femtolasers Rainbow 500, CEP4 module, Femtopower HR 3 kHz; $\lambda_0 = 790\,\mathrm{nm}$, 0.9 mJ pulse energy) are used to seed a neon-filled hollow-core fiber (absolute gas pressure of 2.0 bar) for the generation of an octave-spanning white-light supercontinuum (WLS). The white-light pulses are modulated in the frequency domain using a home-built $4f$ polarization pulse shaper [44–46] specifically adapted to the ultrabroadband WLS [33]. Trichromatic amplitude and phase modulation is implemented by a dual-layer liquid-crystal spatial light modulator (LC-SLM; Jenoptik SLM-640d) and a broadband p polarizer (Codixx colorPol) mounted in the Fourier plane of the $4f$ setup. To achieve highly accurate spectral amplitude and phase modulation, we performed a wavelength-to-pixel calibration utilizing spectral amplitude modulation of individual LC-display pixels in conjunction with a broadband spectrometer [47]. A measured trichromatic spectrum of the resulting PLP field employed in the experiment is shown

in the inset in Fig. 2. The central wavelengths are set to $\lambda_{pu} = 928$ nm (pump), tuned to the two-photon resonance of the $3d$ state, $\lambda_{pr} = 722$ nm (probe) and $\lambda_{ref} = 848$ nm (reference). The spectral FWHMs of the pump (red), probe (blue), and reference (green) pulses are chosen to be $\Delta\omega_{pu} = 0.02$ rad/fs and $\Delta\omega_{pr} = \Delta\omega_{ref} = 0.035$ rad/fs, corresponding to bandwidth-limited pulse durations of $\Delta t_{pu} \approx 139$ fs and $\Delta t_{pr} = \Delta t_{ref} \approx 79$ fs, assuming Gaussian envelopes. The spectral widths $\Delta\omega_{pr}$ and $\Delta\omega_{ref}$ are adapted for optimal energetic overlap of the generated photoelectron wave packets, while the bandwidth of $\Delta\omega_{pu}$ is chosen to be narrower to ensure selective excitation of the $3d$ state [48]. The energetic overlap of the probe and the reference wave packet in the continuum occurs around the kinetic energy $\varepsilon_1 \approx 0.05$ eV [see Fig. 1(a)]. The spectral amplitudes of each color are optimized manually for maximum interference contrast in the SQuaSH channel. To individually advance or delay the pulses in time, we apply linear spectral phase functions using the LC-SLM (see Sec. II and the inset in Fig. 2). Owing to the common-path geometry of the shaper-based scheme, the generated trichromatic pulse sequences are inherently phase locked, allowing for low-jitter and high-precision variation of the relative phases of all three pulses independently [49].

The trichromatic pulse sequences are focused via a spherical mirror ($f = 250$ mm) into the interaction region of a VMI spectrometer [3] filled with K vapor from a dispenser source (Saes Getters). Using a small inclination angle of about $10°$ minimizes the aberrations of our focusing optics. The laser peak intensity of the temporally overlapping trichromatic field is on the order of $I_0 \approx 5 \times 10^{12}$ W/cm^2. The pump pulse alone has an intensity on the order of $I_{pu} \approx 5 \times 10^{11}$ W/cm^2. This estimate results from a measured beam waist of about $28\,\mu$m in the interaction region and the measured pulse durations from Sec. III B. The photoelectron wave packets created by MPI of the K atoms are imaged onto a position-sensitive 2D detector (German Image Detector Systems MCP-77-2-60-P43-CF160-HR) consisting of a dual-layer microchannel plate in the chevron configuration stacked with a phosphor screen. The 2D projections of the PMD are recorded by a CCD camera (Lumenera LW165M). To reconstruct the full 3D PMD, shown in the insets in Figs. 1(a) and 2, we apply photoelectron tomography. To this end, we rotate the input pulse sequence about the laser propagation direction by a superachromatic $\lambda/2$ wave plate [31]. The PMD is retrieved from 45 projections, with an angular step size of $\delta\phi = 4°$, using the Fourier slice algorithm [50] (see [21,35,37,51] for details). The result confirms the cylindrical symmetry of the hologram. Therefore, we employ Abel inversion techniques, based on the PBASEX algorithm, to reconstruct the PMDs from the 2D projections acquired in the different measurements and determine the corresponding energy-resolved photoelectron spectra [see Eq. (8)].

B. Experimental strategy

In this section, we describe our strategy to design and characterize the shaper-generated trichromatic pump-probe-reference pulse sequences employed in the experiment. First, the WLS is compressed using a shaper-based adaptive optimization procedure to maximize the second-harmonic

yield from a thin β-barium borate crystal (Gwu-Lasertechnik, cutting angle $\theta = 29.2°$, $5\,\mu$m thick) [52,53]. The temporal characterization of the pulse sequence is performed *in situ*, i.e., in the interaction region of the VMI spectrometer, by measuring energy-resolved photoelectron spectra from MPI of K as a function of the time delays τ_{pu} and τ_{ref} [46]. In particular, we investigate three-photon frequency mixing of the probe and reference pulses, which results in two different photoelectron signals [35] centered around $\varepsilon_2 \approx 0.30$ eV and $\varepsilon_3 \approx 0.56$ eV. These contributions are referred to as *green-blue* signals. In addition, we investigate the nonresonant frequency mixing of the pump and probe pulses, creating a photoelectron signal around $\varepsilon_6 = \hbar\omega_{pu} + 2\hbar\omega_{pr} - \mathcal{V}_{IP} \approx 0.43$ eV. This signal is denoted as the *red-blue-blue* signal.

First, we perform a time-resolved measurement using only the probe and reference pulses without the pump pulse. In this setup, we vary the time delay of the reference pulse $\tau_{ref} \in [-100\text{ fs}, 100\text{ fs}]$ in steps of $\delta\tau_{ref} = 5$ fs. The time delay of the probe pulse is fixed to $\tau_{pr} = -15$ fs in order to study the influence of the energy-dependent time-evolution phase $\varpi_{holo}(\varepsilon)\tau_{pr}$ [see Eq. (7)] but maintain sufficient temporal overlap between the probe and reference pulses. The latter ensures that the green-blue frequency-mixing signals are still observable in the phase-resolved measurements (see Sec. IV A). The resulting photoelectron spectra $\varrho_{int}(\varepsilon; \tau_{ref})$ are presented in the top frame of Fig. 3(a), showing the two green-blue signals (gray arrows). Both signals are centered temporally around $\tau_{ref} = (-15 \pm 5)$ fs, confirming the time delay of the probe pulse. The bottom frame of Fig. 3(a) depicts energy sections through both green-blue frequency-mixing contributions together with Gaussian fits. The fits have FWHMs of (89 ± 7) fs and (96 ± 6) fs. Since we assume equal pulse durations due to the same spectral widths of the probe and reference pulses, we use the average FWHM of (93 ± 7) fs of these Gaussian fits to determine the pulse durations. Using $\Delta t_{FWHM} = \sqrt{\frac{3}{2}}\Delta t_{pr/ref}$, which is derived from the relation between the multiphoton spectrum and the multiphoton field as discussed in Appendixes A.1. and A.2. in [32], we obtain a pulse duration of $\Delta t_{pr} = \Delta t_{ref} = (76 \pm 6)$ fs, in good agreement with the bandwidth-limited estimation given in Sec. III A.

Next, we perform a time-resolved measurement using the complete trichromatic sequence, which allows for the temporal characterization of the pump pulse. In this measurement, we vary the time delay $\tau_{pu} \in [-215\text{ fs}, 135\text{ fs}]$ in steps of $\delta\tau_{pu} = 8.75$ fs, setting $\tau_{pr} = -15$ fs and $\tau_{ref} = 0$ fs as in the experiment. The resulting photoelectron spectra are depicted in the top panel of Fig. 3(b). In between the green-blue signals centered at ε_2 and ε_3, we additionally observe the red-blue-blue signal around ε_6 (magenta arrow) and a contribution centered at $\varepsilon_5 = \hbar(\omega_{pu} + \omega_{pr} + \omega_{ref}) - \mathcal{V}_{IP} \approx 0.18$ eV (brown arrow). The latter is attributed to trichromatic frequency mixing of the pump, probe, and reference pulses, with each color contributing one photon, and is hence denoted the *red-blue-green* signal. This signal serves to indicate the temporal overlap of all three pulses. However, since the probe and reference pulses are temporally shifted relative to each other, the red-blue-blue signal at ε_6 is better suited to retrieve the FWHM of the pump pulse. The bottom panel of Fig. 3(b) depicts a section through the red-blue-blue signal along with
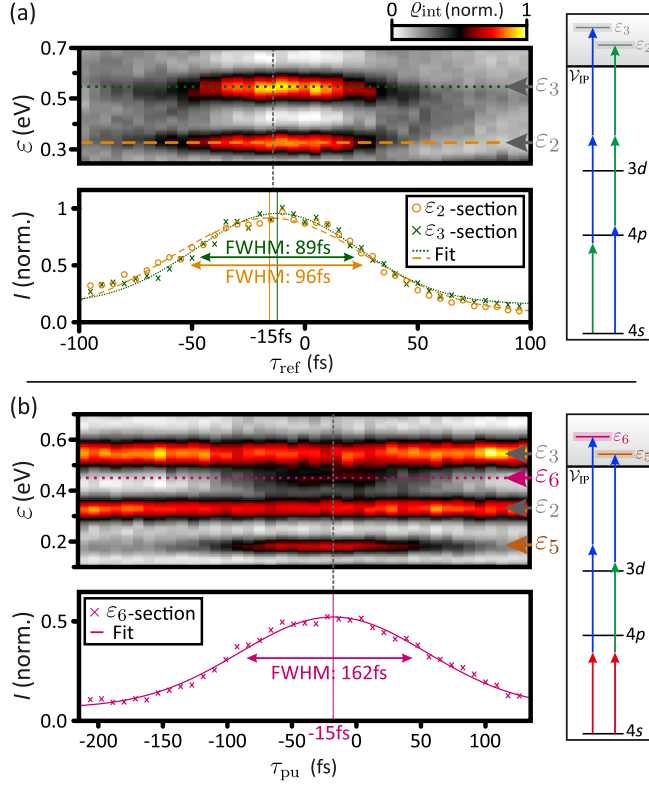
FIG. 3. Time-resolved *in situ* characterization of the laser electric field to temporally characterize the applied pulse sequence. (a) Time-resolved measurement of only the probe (blue) and reference (green) pulses by variation of τ_{ref}. The green-blue frequency-mixing signals at ε_2 and ε_3 are temporally centered around $\tau_{\mathrm{ref}} \approx -15\,\mathrm{fs}$, the time delay of the probe pulse. (b) Time-resolved measurement of the trichromatic pulse sequence by variation of τ_{pu}. The red-blue-blue frequency-mixing signal at ε_6 is also centered around $\tau_{\mathrm{pu}} \approx -15\,\mathrm{fs}$. The frames on the right-hand sides of (a) and (b) show simplified excitation schemes containing only the relevant frequency-mixing terms.

a Gaussian fit. The fit indicates a maximum overlap of both pulses at $\tau_{\mathrm{pu}} = (-15 \pm 5)\,\mathrm{fs}$, again confirming the temporal shift of the probe pulse. With the probe pulse duration Δt_{pr} determined above and an FWHM of $(162 \pm 15)\,\mathrm{fs}$ extracted from the Gaussian fit, we find $\Delta t_{\mathrm{pu}} = (153 \pm 17)\,\mathrm{fs}$. The actual deviations of the measured spectrum in Fig. 2 from a Gaussian shape indicate a slightly larger pulse duration in the experiment. Nevertheless, this result is also in good agreement with the bandwidth-limited estimation from Sec. III A. In the experiment, we separated the pump pulse in time by choosing $\tau_{\mathrm{pu}} = (-215 \pm 7)\,\mathrm{fs}$ in order to reduce the nonresonant frequency-mixing contribution in the photoelectron spectrum and minimize pump-induced Stark shifts during the probe step.

IV. RESULTS AND DISCUSSION

The experiment is performed in two parts. In the first part, we vary the relative phases of all three pulses in the sequence to exert phase control on the photoelectron holo-

gram. We record phase maps $\varrho_{\mathrm{int}}(\varepsilon, \alpha_{\mathrm{v}}; \alpha_0)$ by continuous variation of either φ_{ref} or φ_{pu} and manipulate the phase maps systematically by making use of the remaining phases comprising α_0. The results are presented in Sec. IV A. In the second part, we apply the holographic scheme to investigate dynamic quantum phases imprinted in the hologram by the transient dynamics of the excited atomic system. To this end, we utilize the phase-control results from the first part to remove the phase-insensitive yet energy-dependent background from the phase maps. Evaluation of the corresponding phase contrasts $\mathcal{C}(\varepsilon, \alpha_{\mathrm{v}})$ [see Eq. (9)] highlights the effect of the energy-dependent time-evolution phases on the phase map. In addition, we investigate the dynamic phase accumulated in the bound system due to the detuning of the pump pulse from the atomic resonance by measuring φ_{pr}-resolved phase maps. These results are presented in Sec. IV B.

A. Phase control of the photoelectron hologram

In this first part of the experiment, we study the sensitivity of the photoelectron hologram to the optical phases of each pulse in the trichromatic sequence. For this purpose, we record phase maps by varying the relative phase of either the reference or the pump pulse for different settings of the remaining phases. The time delays $\tau_{\mathrm{pu}} = (-215 \pm 7)\,\mathrm{fs}$ and $\tau_{\mathrm{pr}} = (-15 \pm 5)\,\mathrm{fs}$ are kept fix as described in Sec. III B (see also the inset in Fig. 1). The measured 2D projections of the PMD are Abel inverted, energy calibrated (see Wituschek *et al.* [43] for details), and angularly integrated to obtain the phase map $\varrho_{\mathrm{int}}(\varepsilon, \alpha_{\mathrm{v}}; \alpha_0)$ (see Sec. II). The experimental results are presented in Fig. 4. The top frame in Fig. 4(a) shows the phase map measured by varying $\varphi_{\mathrm{ref}} \in [-\pi, \pi]$ with a step size of $\delta\varphi_{\mathrm{ref}} = 0.13\,\mathrm{rad}$. The remaining phases are set to $\varphi_{\mathrm{pu}} = \varphi_{\mathrm{pr}} = 0$, resulting in $\alpha_0 = 0$. The energy range of the map from $\varepsilon = 0\,\mathrm{eV}$ to $\varepsilon = 0.9\,\mathrm{eV}$ shows all photoelectron contributions in the spectrum. Besides the photoelectron hologram in the SQuaSH channel centered around ε_1, we observe the green-blue signals at ε_2 and ε_3 and the single-color signal created by the probe pulse around ε_4. While the constancy of the blue single-color signal confirms the stability of the experimental system, the green-blue frequency-mixing contributions around ε_2 and ε_3 additionally underscore the amplitude stability of the reference pulse, especially under phase-variations. The hologram, however, is strongly modulated upon variation of φ_{ref}, indicating the efficient manipulation of the interference between the probe and reference wave packets by the relative phase of the reference pulse. The circular insets display measured 2D projections of the PMD for two distinct phases corresponding to maximum constructive interference at $\varphi_{\mathrm{ref}} = -1.64\,\mathrm{rad}$ and maximum destructive interference at $\varphi_{\mathrm{ref}} = -0.64\,\mathrm{rad}$ of both wave packets. The yield modulation of the hologram due to variation of φ_{ref} is periodic, with a period of $2\pi/3$. The periodicity is in accordance with Eqs. (5) and (6) and is due to the fact that the reference wave packet is created via three-photon ionization by the reference pulse. Hence, the periodicity of the phase map with respect to the variation of an optical phase provides information about the ionization dynamics, e.g., the role of the corresponding subpulse in the MPI process. Small deviations in the periodicity of the modulation are attributed
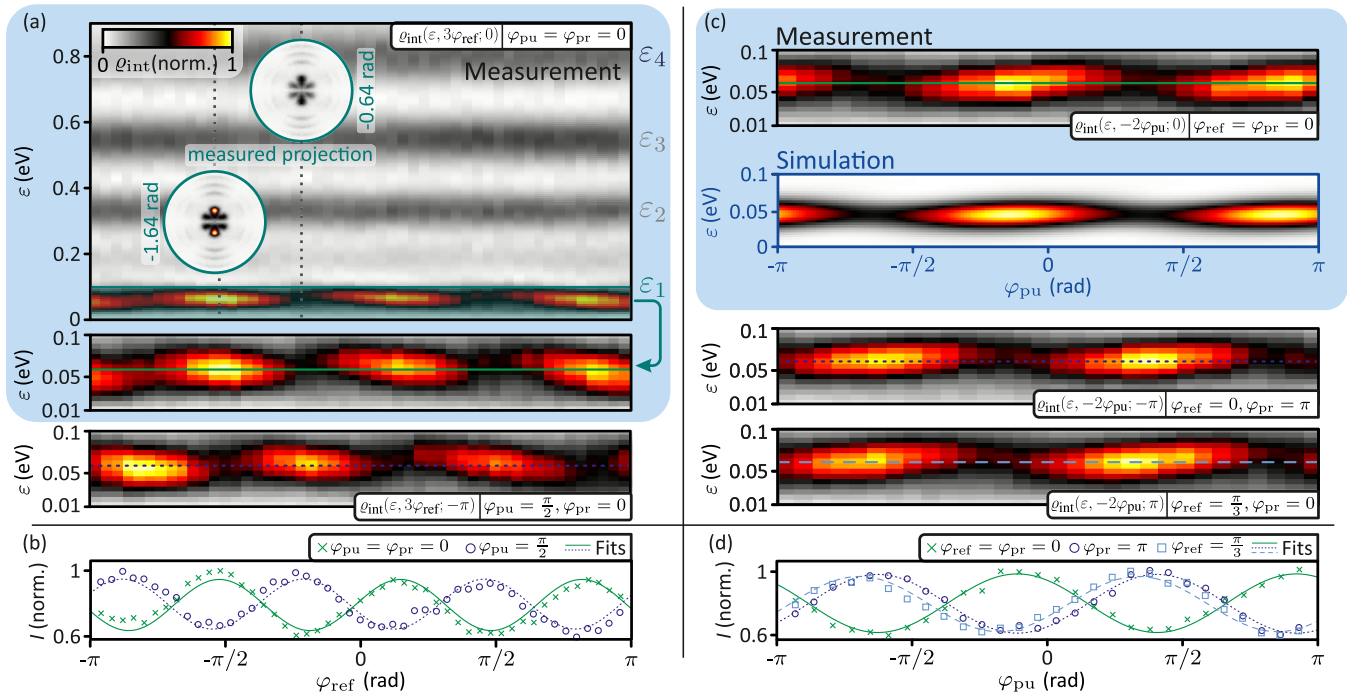
FIG. 4. Phase-sensitive photoelectron hologram from trichromatic SQuaSH of a (2+1) REMPI and a nonresonant three-photon ionization pathway. (a) Measured phase map $\varrho_{\text{int}}(\varepsilon, 3\varphi_{\text{ref}}; 0)$ for the relative optical phase φ_{ref} of the reference pulse in the energy windows of $\varepsilon \in [0, 0.9]\,\text{eV}$ (top frame) and $\varepsilon \in [0.01, 0.1]\,\text{eV}$ (middle frame) for $\varphi_{\text{pu}} = \varphi_{\text{pr}} = 0$. Besides the frequency mixing (ε_2 and ε_3) and single-color (ε_4) contributions in the top frame, we observe a pronounced interference pattern around ε_1 with a $\frac{2\pi}{3}$ periodicity resulting from wave-packet interferences according to Eq. (5). The insets depict measured and energy-calibrated PMDs at $\varphi_{\text{ref}} = -1.64\,\text{rad}$ (left) and $-0.64\,\text{rad}$ (right). In the bottom frame of (a) we show $\varrho_{\text{int}}(\varepsilon, 3\varphi_{\text{ref}}; -\pi)$, i.e., the inverted interference structure which is generated by applying $\varphi_{\text{pu}} = \frac{\pi}{2}$. (b) Sections through the interference patterns of (a) (crosses and circles) together with cosine fits (solid and dotted lines), emphasizing the sinusoidal behavior according to Eq. (5). (c) Same as (a), but for a phase map $\varrho_{\text{int}}(\varepsilon, -2\varphi_{\text{pu}}; \alpha_0)$ regarding the relative phase φ_{pu}. The two frames at the top of (c) show the measured and simulated φ_{pu} phase maps $\varrho_{\text{int}}(\varepsilon, -2\varphi_{\text{pu}}; 0)$ with a periodicity of π for $\varphi_{\text{ref}} = \varphi_{\text{pr}} = 0$. The bottom two frames show $\varrho_{\text{int}}(\varepsilon, -2\varphi_{\text{pu}}; -\pi)$ and $\varrho_{\text{int}}(\varepsilon, -2\varphi_{\text{pu}}; \pi)$, i.e., the inverted interferences using either $\varphi_{\text{pr}} = \pi$ or $\varphi_{\text{ref}} = \frac{\pi}{3}$. (d) Sections through the measured phase maps of (c) (crosses, squares, and circles) together with cosine-fits (solid, dashed, and dotted lines).

to slight spectral amplitude modulations due to diffraction at the discrete phase pattern applied to the pixelated LC-SLM [54,55]. The phase map in the middle frame of Fig. 4(a) shows a magnification of the relevant SQuaSH channel. In this representation, we see not only that the hologram is modulated in yield but that the lobes of the interference pattern are also tilted. The tilt indicates the energy-dependent quantum phase $\varepsilon\tau/\hbar$ [see Eq. (7)] due to the free time evolution of the probe wave packet prior to the creation of the reference wave packet. A closer investigation of this tilt is the subject of Sec. IV B 1. Next, we manipulate the interference pattern by setting the relative phase of the pump pulse to $\varphi_{\text{pu}} = \pi/2$. Since the pump contributes two photons to the hologram generation [see Fig. 1(a)], this additional optical phase is expected to shift the interference pattern by $\alpha_0 = \pi$ [see Eq. (6)]. The π phase shift is confirmed by the measured phase map shown in the bottom frame of Fig. 4(a), which is inverted relative to the one shown in the middle frame. To emphasize this inversion, we plot sections through both maps along the phase axis at $\varepsilon = 0.06\,\text{eV}$ in Fig. 4(b), together with cosine fits through the data. The fits reproduce the $2\pi/3$ periodicity of the oscillations and emphasize the antiphase relation of the two measured phase maps with a measured phase shift of $\Delta\varphi_{\text{ref,exp}} = (3.1 \pm 0.1)\,\text{rad}$.

In the next step, we vary the relative phase of the pump pulse continuously in the range $\varphi_{\text{pu}} \in [-\pi, \pi]$ with a step size of $\delta\varphi_{\text{pu}} = 0.21\,\text{rad}$, set $\varphi_{\text{ref}} = \varphi_{\text{pr}} = 0$, and record the phase map $\varrho_{\text{int}}(\varepsilon, -2\varphi_{\text{pu}}; 0)$. The experimental result is presented in the top frame of Fig. 4(c). Below, we compare the experimental results to a numerical simulation. The calculation is based on the numerical solution of the time-dependent Schrödinger equation for the perturbative interaction of a hydrogenlike four-level atom, including the potassium ground state $4s$ and the excited states $4p$, $5s$, and $3d$, with a sequence of three Gaussian-shaped pulses similar to those used in the experiment. Building on the numerically calculated bound-state population dynamics, the energy-resolved photoelectron spectra are calculated using time-dependent perturbation theory (see, e.g., [56] for a more detailed description). The simulation result agrees very well with the measured phase map. Both display a pronounced yield oscillation of the hologram as a function of φ_{pu} with a period of $2\pi/2 = \pi$. This period is expected from Eq. (6) since the pump pulse excites the $3d$ state by absorption of two photons (see also the discussion above). The absolute phase in the simulation was adapted to reproduce the measured data. To demonstrate the full controllability of the photoelectron hologram via the phases of all three pulses, we repeated the measurement for either $\varphi_{\text{pr}} = \pi$

or $\varphi_{\text{ref}} = \pi/3$. According to Eq. (6), these settings result in $\alpha_0 = -\pi$ and $\alpha_0 = \pi$, respectively. Hence, both settings are expected to invert the interference pattern, which is confirmed by the recorded phase maps shown in the two bottom frames of Fig. 4(c). The inversion is emphasized by direct comparison of sections taken through the measured phase maps at $\varepsilon = 0.06$ eV and is depicted in Fig. 4(d). The measured phase shifts are $\Delta\varphi_{\text{pu,exp}} = -(3.1 \pm 0.2)$ rad and $\Delta\varphi_{\text{pu,exp}} = (3.3 \pm 0.2)$ rad, respectively. The minor phase shift between the two inverted phase maps [light blue dashed and dark blue dotted lines in Fig. 4(d)] is within the estimated errors of ± 0.2 rad. The good agreement of the measured phase maps with the theoretical prediction and the simulation results highlights the fidelity of the trichromatic SQuaSH scheme regarding its phase stability and shows the potential to optically manipulate the photoelectron hologram, which will be utilized in the next part of the experiment.

B. Analysis of dynamic quantum phases

In the second part of the experiment, we investigate dynamic quantum phases originating from the free time evolution $\beta_{\text{f}}(k) = \varpi_{\text{holo}}(k)\tau_{\text{pr}}$ of the created probe wave packet in the continuum prior to the creation of the reference wave packet (Sec. IV B 1), as well as the phase $\beta_{\text{b}} = \varpi_{\text{pu}}\tau_{\text{pu}}$ associated with the time evolution in the bound system after the excitation by the pump pulse (Sec. IV B 2). The former induces an energy-dependent phase which shears the entire interference pattern along the phase axis, whereas the latter results in a constant phase shift of the interference pattern, similar to the relative optical phases in Sec. IV A. In addition, we show that a time-resolved measurement of the photoelectron hologram by variation of τ_{pu} reveals a beating of the $3d$ state with the second harmonic of the pump pulse, which is highly sensitive to the pump detuning ϖ_{pu}.

1. Time evolution of the probe wave packet

We start with the analysis of the time-evolution phase accumulated by the probe photoelectron wave packet after its creation by the probe pulse and before the generation of the reference wave packet ($\tau_{\text{ref}} = 0$ fs). Because each continuum state contributing to the probe wave packet accumulates a different time-evolution phase $\varepsilon\tau_{\text{pr}}/\hbar$, the resulting phase $\beta_{\text{f}}(k)$ imprinted in the hologram [see Eq. (7)] depends linearly on the photoelectron energy ε. This linear radial phase results in the shearing of the interference pattern observed in the recorded phase maps in Figs. 4(a) and 4(c). For a background-free analysis of this shearing—and hence of the energy-dependent time-evolution phase of the probe wave packet—we determine the corresponding phase contrasts $\mathcal{C}(\varepsilon, \alpha_{\text{v}})$ according to Eq. (9). The experimental results are shown in Fig. 5 and compared to the results of the numerical simulation. The experimental phase contrast $\mathcal{C}(\varepsilon, 3\varphi_{\text{ref}})$ in Fig. 5(a) is derived from the two phase maps in Fig. 4(a), while the phase contrast $\mathcal{C}(\varepsilon, -2\varphi_{\text{pu}})$ in Fig. 5(b) is calculated using the first and third ($\varphi_{\text{ref}} = \pi/3$) phase maps from Fig. 4(c). Both phase contrasts exhibit modulations of about 50% and display a tilt of the interference lobes with a negative slope [Fig. 5(a)] and a positive slope [Fig. 5(b)]. For a theoretical description of these slopes, we consider the position of the
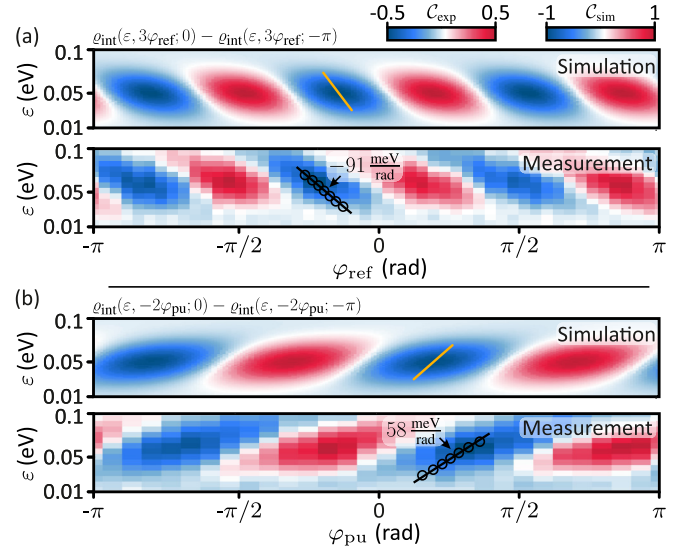

FIG. 5. Measured and simulated phase contrasts $\mathcal{C}(\varepsilon, \alpha_{\text{v}})$ of the phase maps from Fig. 4, according to Eq. (9). (a) corresponds to the φ_{ref} phase maps from Fig. 4(a) (second and third frames), and (b) is calculated from the φ_{pu} phase maps in Fig. 4(c) (first and third frames). The black circles correspond to the extracted maxima at each energy section, and the orange solid lines represent the theoretical delay-induced tilt according to Eq. (10). The slopes of the interference fringes (indicated in black) and the extracted delay of $\tau_{\text{pr}} \approx -22$ fs are in good agreement with theoretical results from Sec. IV B 1 and the measurements from Sec. III B. For the simulations and the calculation of the theoretical slopes we assumed a time delay of $\tau_{\text{pr}} = -15$ fs.

interference lobes, i.e., the maxima of the density in Eq. (5), on the phase axis as a function of ε, analogous to the treatment in [22,37,57]. The relation between the photoelectron kinetic energy of the interference lobes and the optical phases reads (see Appendix B)

$$\varepsilon = \frac{\hbar}{\tau_{\text{pr}}}(3\varphi_{\text{ref}} - 2\varphi_{\text{pu}} - \varphi_{\text{pr}}). \tag{10}$$

Thus, we find slopes of $m_{\text{ref}} = 3\hbar/\tau_{\text{pr}}$ and $m_{\text{pu}} = -2\hbar/\tau_{\text{pr}}$ for the phase contrasts recorded upon variation of φ_{ref} and φ_{pu}, respectively. Note the negative time delay of the probe pulse, i.e., $\tau_{\text{pr}} < 0$. The different signs of the slopes result from the fact that the relative phases of the pump and reference pulse are introduced in different ionization pathways. The slopes derived from the theoretical model are indicated as orange lines in the corresponding simulation in Fig. 5. Black circles indicate the slopes of the measured phase contrasts. Assuming $\tau_{\text{pr}} = (-15 \pm 5)$ fs, Eq. (10) predicts slopes of $m_{\text{ref}} = (-132 \pm 44)$ meV/rad and $m_{\text{pu}} = (88 \pm 29)$ meV/rad. The slopes of the measured contrasts, extracted from linear fits indicated as black lines in Fig. 5, are $m_{\text{ref,exp}} = (-91 \pm 19)$ meV/rad and $m_{\text{pu,exp}} = (58 \pm 8)$ meV/rad. The corresponding probe-pulse time delay is $\tau_{\text{pr}} = (-22 \pm 4)$ fs. These results are in reasonable agreement with the theoretical model and in accordance with the characterization results from Sec. III B taking into account the energy resolution of the VMI and the error of the measured pulse delays. Besides these errors, a minor systematic error
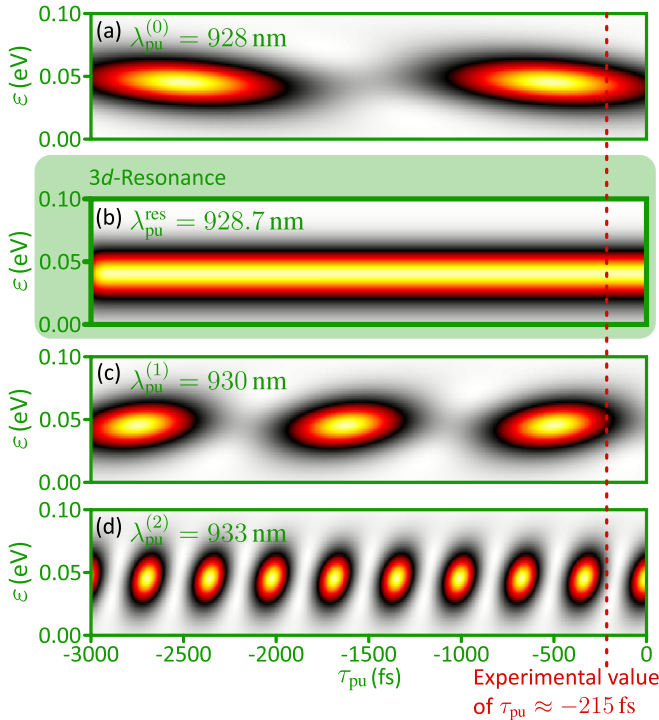
FIG. 6. Simulated time-resolved studies of the bound time evolution of the 3d state for different central wavelengths of the pump pulse, resulting in different beatings between the pump pulse and the atomic oscillation. While a near-resonant excitation of the 3d state in (a), (c), and (d) leads to a pronounced beating pattern with the corresponding frequencies ϖ_{pu}, resonant excitation in (b) yields a constant signal in accordance with $\varpi_{pu} = 0$. The tilts of the lobes in the interference patterns indicate the direction of the detuning and change from the blue-detuned case in (a) to the red-detuned cases in (c) and (d).

in the energy calibration may also affect the reconstructed slopes.

These findings show that, besides the period of the recorded phase maps, phase-sensitive information on the ionization dynamics is imprinted in the tilt of the interference pattern, similar to what was found in [22,37,57]. Our method utilizing the optical phases to invert the interference pattern allows for the background-free investigation, as exemplified by the quantitative analysis of the observed results.

2. Time evolution of the bound state

Next, we examine the influence of dynamic quantum phases that are accumulated in the bound system on the hologram. After the excitation by the pump pulse, the excited 3d state undergoes a field-free time evolution with eigenfrequency ω_{3d} until the second pulse probes the population. In a time-resolved study using an interferometer, this time evolution manifests as a phase of $\omega_{3d}(\tau_{pr} - \tau_{pu})$. In this case, a variation of either the pump or the probe time delay leads to a fast yield oscillation of the hologram with a frequency of ω_{3d}, corresponding to a period of about 1.5 fs. In contrast, our shaper-based approach permits us to temporally shift only the pulse envelope instead of the entire pulse by applying the linear phases relative to the respective central frequen-

cies [38,39] [see Eq. (2)]. The additionally acquired phase of $2\omega_{pu}\tau_{pu}$ partially compensates for the phase of the atomic oscillation. This manifests in the reduced time-evolution phase in Eq. (5) given by $\beta_b = 2\omega_{pu} - \omega_{3d} \equiv \varpi_{pu}\tau_{pu}$ [see Eq. (7)]. Thus, the oscillation in Fig. 6 shows a slow beating with frequency ϖ_{pu} [21] between the pump pulse and the natural atomic oscillation of the 3d state, instead of the eigenfrequency ω_{3d}. Analogous to a stroboscopic experiment, where the frequency of the stroboscope is matched to a rapid oscillatory process, a slight detuning between the two (represented in our experiment by ϖ_{pu}) reveals a much slower and easily detectable dynamics. Knowledge of the stroboscopic frequency then allows us to reconstruct the process dynamics. Figure 6 shows τ_{pu}-resolved simulations of the beating for different two-photon detunings of the pump pulse from the 3d state. On resonance ($\lambda_{pu}^{res} = 928.7$ nm, $\varpi_{pu} = 0$), no signature of the 3d time evolution is imprinted in the τ_{pu}-resolved map shown in Fig. 6(b). For the detuned case ($\varpi_{pu} \neq 0$), we vary the central wavelength of the pump pulse in three steps, $\lambda_{pu}^{(0)} = 928$ nm (blue detuned) and $\lambda_{pu}^{(1)} = 930$ nm and $\lambda_{pu}^{(2)} = 933$ nm (both red detuned). The corresponding beating periods of $T^{(0)} = 1964$ fs, $T^{(1)} = 1122$ fs, and $T^{(2)} = 308$ fs are reproduced in the simulated τ_{pu}-resolved spectra shown in Figs. 6(a), 6(c) and 6(d), respectively. Thus, the beating frequency of the signal, associated with the dynamic of interest, can be adapted to the resolution of the measurement. The vanishing of the modulation in the time-resolved measurement for $\varpi_{pu} = 0$ allows us to experimentally fine-tune the laser field to the resonance of the system.

Here, we study the beating by analyzing the phase maps analogous to the results in Sec. IV A. The measured phase maps for the fixed pump time delay of $\tau_{pu} \approx -215$ fs allow us to retrieve the phase shifts between the lobes in Fig. 6 (red dashed vertical line). To this end, we vary φ_{pr} to extract the phase shifts (modulo 2π) as described by Eq. (6). This procedure also complements the demonstration of phase control discussed in Sec. IV A by using the relative phase of the probe pulse as α_v. Figure 7 shows the phase maps $\varrho_{int}(\varepsilon, -\varphi_{pr}; 0)$ corresponding to the previous chosen wavelengths with $\varphi_{pr} \in [-\pi, \pi]$ and a step size of $\delta\varphi_{pr} = 0.21$ rad while setting $\varphi_{pu} = \varphi_{ref} = 0$. Figures 7(a)–7(c) depict the phase maps recorded for $\lambda_{pu}^{(0)}$, $\lambda_{pu}^{(1)}$, and $\lambda_{pu}^{(2)}$. Sections taken at $\varepsilon = 0.06$ eV are shown in Fig. 7(d) together with the respective cosine fits for a quantitative analysis. Comparison of the different sections reveals a pronounced phase shift of the interference patterns in Figs. 7(b) and Fig. 7(c) compared to Fig. 7(a). The phase shifts $\Delta\varphi_{pr,exp}$ obtained from the cosine fits in Fig. 7(d), indicated by red circles, are given in Table I (second column). The phase shift $\Delta\varphi_{pr,theo}$ for the variation of the pump pulse frequency $\Delta\omega_{pu}$ is derived from the theoretical model in Appendix B as

$$\Delta\varphi_{pr,theo} = 2\Delta\omega_{pu}\tau_{pu}. \tag{11}$$

The factor of 2 is due to the two-photon excitation of the 3d state by the pump pulse. The theoretical phase shifts determined with Eq. (11) are presented in the third column of Table I. Both values are in good agreement with the extracted phase shifts from the measured data. These results underscore the fidelity of the shaper-based scheme regarding the fine tunability of the colors in the trichromatic field and the
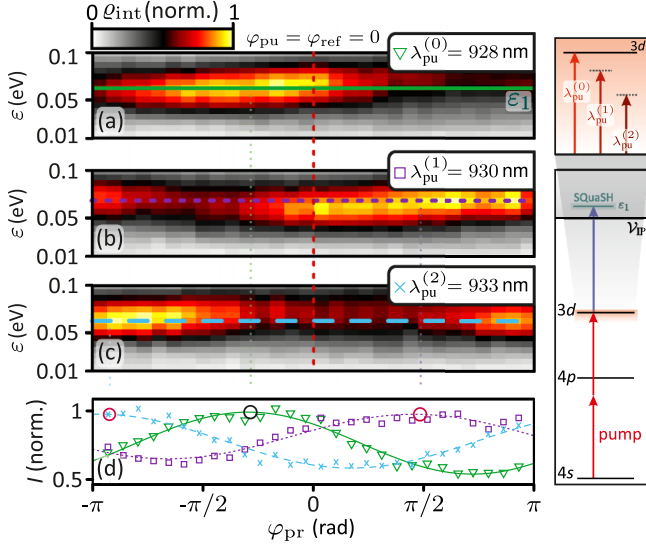
FIG. 7. Measured phase maps $\varrho_{\text{int}}(\varepsilon, -\varphi_{\text{pr}}; 0)$ and extracted phase shifts due to a variation of the central wavelength λ_{pu} of the pump pulse. (a)–(c) The energy-resolved phase maps for $\lambda_{\text{pu}}^{(0)} = 928$ nm, $\lambda_{\text{pu}}^{(1)} = 930$ nm, and $\lambda_{\text{pu}}^{(2)} = 933$ nm exhibit a 2π periodicity. (d) Energy sections at ε_1 of the measured phase maps in (a)–(c) (crosses, squares, and triangles) together with corresponding cosine fits (solid, dashed, and dotted lines). The detuning-induced phase shifts relative to the resonant case (black circle) are highlighted by red circles. The red dashed line corresponds to the red dashed line in Fig. 6 and indicates the τ_{pu} section in the simulated time-resolved studies.

precise retrieval of quantum-mechanical phases from the created hologram.

V. SUMMARY AND CONCLUSION

In this paper, we presented a trichromatic shaper-based quantum state holography (SQuaSH) scheme to measure phase-sensitive multiphoton ionization (MPI) dynamics. The trichromatic scheme builds on the shaper-based bichromatic pump-probe technique introduced in [30] and extends the self-referenced bichromatic holography technique reported in [21] by introducing an independent reference pulse with a third color. The concept is based on the use of trichromatic pump-probe-reference pulse sequences, with the central frequencies chosen such that $N_{\text{pu}}\omega_{\text{pu}} + N_{\text{pr}}\omega_{\text{pr}} = N_{\text{ref}}\omega_{\text{ref}}$ in order to ensure energetic overlap in the continuum. In an $(N_{\text{pu}} + N_{\text{pr}})$ resonance-enhanced MPI (REMPI) process, the pump pulse resonantly excites bound-state dynamics which are subse-

TABLE I. Theoretical and experimentally extracted relative phase shifts $\Delta\varphi_{\text{pr,exp}}$ and $\Delta\varphi_{\text{pr,theo}}$ of the SQuaSH channel interferences in a phase map $\varrho_{\text{int}}(\varepsilon, -\varphi_{\text{pr}}; 0)$ due to the variation of the pump-pulse wavelength λ_{pu}. The theoretical phase shifts were calculated according to Eq. (11).

Detuning	λ_{pu} (nm)	$\Delta\varphi_{\text{pr,exp}}$ (rad)	$\Delta\varphi_{\text{pr,theo}}$ (rad)
(1)	930 ± 0.8	2.18 ± 0.30	1.89 ± 0.06
(2)	933 ± 0.8	4.60 ± 0.30	4.69 ± 0.15

quently mapped into the continuum by the probe pulse. The created probe photoelectron wave packet interferes with a reference wave packet from direct N_{ref}-photon ionization of the ground state by the reference pulse. In the experiment, we combined trichromatic white-light supercontinuum pulse shaping with photoelectron velocity map imaging (VMI) and measured energy- and angle-resolved photoelectron spectra. For the analysis, the experiments were complemented by a theoretical model of perturbative trichromatic MPI of a one-electron atom and by numerical simulations based on the short-time propagation of the time-dependent Schrödinger equation for a multilevel atom interacting with a trichromatic laser field. We demonstrated the trichromatic SQuaSH scheme on the $(2 + 1)$ REMPI of potassium atoms using shaper-generated parallel linearly polarized trichromatic pump-probe-reference sequences. Two-photon excitation of the potassium $3d$ state by the pump pulse was mapped into the continuum by one-photon ionization with the time-delayed probe pulse. The probe wave packet was superimposed by a reference wave packet created by nonresonant three-photon ionization of the $4s$ ground state by the reference pulse. The photoelectron momentum distribution (PMD) of the resulting hologram was reconstructed from the measured VMI images using Abel inversion. We first demonstrated phase control of the hologram by systematic variation of the relative phases of all three pulses in the trichromatic sequence. The measured phase maps, i.e., energy-resolved photoelectron spectra recorded as a function of the different optical phases, exhibited high-contrast interference patterns. The characteristic periodicity observed in the SQuaSH channel of the hologram unambiguously revealed the number of photons of each color required for MPI, i.e., *one blue* photon and *two red* photons versus *three green* photons. In the second step, we applied the holographic scheme to investigate quantum phases imprinted in the hologram. Our approach enabled background-free examination of time-evolution phases accumulated in the continuum by the probe wave packet via the shearing of the interference pattern. In contrast, the time-evolution phase accumulated in the bound system by the excited $3d$ state introduced a constant phase, resulting in an overall shift of the interference pattern. The experimental results were in good agreement with our numerical simulation and consistent with the theoretical model.

In conclusion, the shaper-based trichromatic holography scheme introduced here is a powerful tool for the phase-sensitive investigation of ultrafast quantum dynamics in atoms and molecules. Due to the common-path geometry, pump, probe, and reference pulses are inherently phase locked, ensuring a maximum interference contrast in the measured phase maps. Independent control of the phase, the time delay, and the central wavelength of all three pulses renders the shaper-based approach very versatile and adaptable to various applications. Our results for the potassium model system show that the structure of the interference pattern contains detailed phase information about the underlying bound and free ionization dynamics.

Possible applications of the scheme include shaper-based multidimensional spectroscopy [58,59] and the time-resolved holographic imaging of nonadiabatic molecular dynamics [60]. Polarization-tailored [33] trichromatic pump-probe-

reference sequences will be useful for studying *polarization*-sensitive MPI dynamics, such as spin-orbit wave-packet dynamics in atoms [29] and vibronic wave-packet dynamics in molecules [61]. In these cases, the phase information imprinted in the angular distribution of the hologram will reveal additional information on the dynamics. In general, the use of polarization-shaped pulses for trichromatic SQuaSH breaks the cylinder symmetry of the PMD, requiring tomographic techniques [31] for its 3D reconstruction. Trichromatic SQuaSH will enable the investigation of more complex (phase) dynamics, e.g., time delays in strong-field ionization of atoms [62] and geometrical phases in the nonadiabatic electron-nuclear dynamics at conical intersections in molecules [63]. Also the development of SQuaSH for the nonperturbative interaction regime and its application to the selective population of dressed states [64] is currently being investigated in our labs.

ACKNOWLEDGMENT

APPENDIX A: THEORETICAL DESCRIPTION OF PHOTOELECTRON HOLOGRAMS FROM TRICHROMATIC SQuaSH

The trichromatic pump-probe-reference pulse sequence described by Eq. (3) induces the interference of two $f(m = 0)$-type photoelectron wave packets with angular distribution $\psi_{3,0}(\theta, \phi) \propto Y_{3,0}(\theta, \phi)$. The superposition wave function in the momentum representation and spherical coordinates $\boldsymbol{k} = (k, \theta, \phi)$ is written as

$$\Psi(\boldsymbol{k}) \propto [a_{\mathrm{ref}}(k) + a_{\mathrm{pr}}(k)]\psi_{3,0}(\theta, \phi), \quad \text{(A1)}$$

where $a_{\mathrm{ref}}(k)$ and $a_{\mathrm{pr}}(k)$ describe the amplitudes of the reference and probe wave packets, respectively. These amplitudes describe the radial part of the resulting photoelectron hologram. In the weak-field limit, the amplitudes $a_{\mathrm{ref}}(k)$ and $a_{\mathrm{pr}}(k)$ are calculated using third-order time-dependent perturbation theory [21,65–67]. Initially, the $3d$ state is excited by the pump pulse by two-photon absorption, leading to a time-dependent amplitude of [21]

$$d(t) = \frac{\mu_{ds}^{(2)}}{(i\hbar)^2} \int_{-\infty}^{t} \mathcal{E}_{\mathrm{pu}}^2(t' - \tau_{\mathrm{pu}})e^{-i[\varpi_{\mathrm{pu}}t' - 2\varphi_{\mathrm{pu}}]}dt' \quad \text{(A2)}$$

and hence to a final amplitude of

$$\lim_{t \to \infty} d(t) = d^\infty = \frac{\mu_{ds}^{(2)}}{(i\hbar)^2}\tilde{\mathcal{E}}_{\mathrm{pu}}^{(2)}(\varpi_{\mathrm{pu}})e^{-i\varpi_{\mathrm{pu}}\tau_{\mathrm{pu}}}e^{2i\varphi_{\mathrm{pu}}}, \quad \text{(A3)}$$

where $\mu_{ds}^{(2)}$ describes the effective two-photon transition dipole moment between the ground state and the $3d$ state. Further, we introduced the pump detuning

$$\varpi_{\mathrm{pu}} = 2\omega_{\mathrm{pu}} - \omega_{3d} \quad \text{(A4)}$$

with respect to the $3d$ resonance. In the next step the resulting $3d$-state population is mapped by the probe pulse via one-photon ionization into an f-type continuum with a final

amplitude of

$$a_{\mathrm{pr}}(k) = \frac{\mu_{kd}}{i\hbar}d^\infty(\tau_{\mathrm{pu}})\int_{-\infty}^{\infty}\mathcal{E}_{\mathrm{pr}}(t - \tau_{\mathrm{pr}})e^{-i[\varpi_{\mathrm{pr}}t - \varphi_{\mathrm{pr}}]}dt$$
$$= c_{\mathrm{pr}}(k)e^{-i(\varpi_{\mathrm{pu}}\tau_{\mathrm{pu}} + \varpi_{\mathrm{pr}}\tau_{\mathrm{pr}})}e^{i(2\varphi_{\mathrm{pu}} + \varphi_{\mathrm{pr}})}, \quad \text{(A5)}$$

using

$$\varpi_{\mathrm{pr}}(k) = \omega_{\mathrm{pr}} - \omega_k - \omega_{\mathrm{IP}} + \omega_{3d}. \quad \text{(A6)}$$

After the time τ_{pr}, since the probe is advanced in time, the reference wave packet is generated by nonresonant three-photon ionization of the $4s$ ground state into an f-type continuum. The final amplitude of the reference wave packet reads

$$a_{\mathrm{ref}}(k) = \frac{\mu_{ks}^{(3)}}{(i\hbar)^3}\int_{-\infty}^{\infty}\mathcal{E}_{\mathrm{ref}}^3(t - \tau_{\mathrm{ref}})e^{-i(\varpi_{\mathrm{ref}}t - 3\varphi_{\mathrm{ref}})}dt$$
$$= c_{\mathrm{ref}}(k)e^{-i\varpi_{\mathrm{ref}}\tau_{\mathrm{ref}}}e^{3i\varphi_{\mathrm{ref}}}, \quad \text{(A7)}$$

with

$$\varpi_{\mathrm{ref}}(k) = 3\omega_{\mathrm{ref}} - \omega_k - \omega_{\mathrm{IP}}. \quad \text{(A8)}$$

Note that, owing to the condition $3\omega_{\mathrm{ref}} = \omega_{3d} + \omega_{\mathrm{pr}}$ for the energetic overlap of the interfering wave packets, we find the detuning

$$\varpi_{\mathrm{holo}}(k) := \varpi_{\mathrm{ref}}(k) \equiv \varpi_{\mathrm{pr}}(k). \quad \text{(A9)}$$

Finally, the photoelectron hologram is written as

$$\Psi(\boldsymbol{k}) \propto (c_{\mathrm{ref}}(k)e^{-i\varpi_{\mathrm{holo}}(k)\tau_{\mathrm{ref}}}e^{3i\varphi_{\mathrm{ref}}}$$
$$+ c_{\mathrm{pr}}(k)e^{-i[\varpi_{\mathrm{pu}}\tau_{\mathrm{pu}} + \varpi_{\mathrm{holo}}(k)\tau_{\mathrm{pr}}]}e^{i(2\varphi_{\mathrm{pu}} + \varphi_{\mathrm{pr}})})\psi_{3,0}(\theta, \phi). \quad \text{(A10)}$$

Introducing the real-valued shorthand notations $B(k) = |c_{\mathrm{ref}}(k)|^2 + |c_{\mathrm{pr}}(k)|^2$ and $S(k) = 2|c_{\mathrm{ref}}(k)||c_{\mathrm{pr}}(k)|$, we obtain the electron density $\varrho(\boldsymbol{k}) = |\Psi(\boldsymbol{k})|^2$ as

$$\varrho(\boldsymbol{k}) \propto [B(k) + S(k)\cos(\alpha_{\mathrm{opt}} + \beta(k) + \gamma_{\mathrm{qm}})]|\psi_{3,0}(\theta, \phi)|^2, \quad \text{(A11)}$$

with the phases

$$\alpha_{\mathrm{opt}} = 3\varphi_{\mathrm{ref}} - 2\varphi_{\mathrm{pu}} - \varphi_{\mathrm{pr}}, \quad \text{(A12)}$$

$$\beta(k) = \varpi_{\mathrm{pu}}\tau_{\mathrm{pu}} + \varpi_{\mathrm{holo}}(k)(\tau_{\mathrm{pr}} - \tau_{\mathrm{ref}})$$
$$\equiv \beta_{\mathrm{b}} + \beta_{\mathrm{f}}(k), \quad \text{(A13)}$$

and $\gamma_{\mathrm{qm}} = \chi_{\mathrm{ref}} - \chi_{\mathrm{pr}}$, where χ_{ref} and χ_{pr} describe the phases of the corresponding amplitudes c_{ref} and c_{pr}. In Eq. (A13), we identify the phases $\beta_{\mathrm{b}} = \varpi_{\mathrm{pu}}\tau_{\mathrm{pu}}$ and $\beta_{\mathrm{f}}(k) = \varpi_{\mathrm{holo}}(k)(\tau_{\mathrm{pr}} - \tau_{\mathrm{ref}})$ with the bound and free time evolutions of the system, respectively. The electron density in Eq. (A11) describes a yield modulation around the energy $\varepsilon = \hbar\omega_k$ dependent on the optical phases φ_{pr}, φ_{pu}, and φ_{ref} as well as the dynamic quantum phases β_{b} and $\beta_{\mathrm{f}}(k)$. In the experiment, we use $\tau_{\mathrm{ref}} = 0$ fs as the time zero.

APPENDIX B: THEORETICAL DESCRIPTION OF FREE AND BOUND-STATE TIME EVOLUTIONS

To investigate the free and bound time evolutions of the electron wave packet, we consider the maxima of the density in Eq. (A11). To incorporate a frequency variation of the pump

pulse $\Delta\omega_{\mathrm{pu}} = \omega_{\mathrm{pu}}^{(1)/(2)} - \omega_{\mathrm{pu}}^{(0)}$ we adapt Eq. (A13), resulting in the condition for constructive interference

$$2\Delta\omega_{\mathrm{pu}}\tau_{\mathrm{pu}} + \beta_{\mathrm{b}} + \beta_{\mathrm{f}}(k) + \alpha_{\mathrm{opt}} = 2\pi n - \gamma_{\mathrm{qm}}, \qquad \text{(B1)}$$

with $n \in \mathbb{Z}$ and $\omega_{\mathrm{pu}}^{(0)} = 2.03 \,\mathrm{rad/fs}$. The first term in Eq. (B1) represents the modified beating phase between the bound-state time evolution and the laser electric field. This beating modification allows us to tune the laser field to a specific bound-state dynamics of interest. While the bound-state dynamics itself is very fast and thus difficult to detect in a time-resolved measurement, the modified photoelectron beating signal is significantly slower and requires a much lower temporal resolution for its retrieval (see Sec. IV B 2).

All relative optical phases are incorporated in the quantity α_{opt}. The term β_{b} represents a constant phase offset originating from the bound-state time evolution, whereas the term $\beta_{\mathrm{f}}(k)$, describing the free time evolution, also exhibits an additional k dependence, resulting in a tilt of the interference fringes in the phase map. Setting $\tau_{\mathrm{ref}} = 0 \,\mathrm{fs}$ as in the experiment and omitting the constant phase terms on the right-hand side of Eq. (B1), we obtain

$$2\Delta\omega_{\mathrm{pu}}\tau_{\mathrm{pu}} + \varpi_{\mathrm{pu}}\tau_{\mathrm{pu}} + \varpi_{\mathrm{holo}}(k)\tau_{\mathrm{pr}} = -\alpha_{\mathrm{opt}}, \qquad \text{(B2)}$$

using the definitions in Eq. (A13).

a. Free time evolution. First, we study the influence of the free time evolution introduced by a nonvanishing time delay τ_{pr}, assuming that the pump pulse is tuned on resonance,

i.e., $\varpi_{\mathrm{pu}} = 0$. The application of Eq. (B2) leads to a relation between the photoelectron kinetic energy $\varepsilon = \hbar\omega_k$ and the relative optical phases

$$\varepsilon = \frac{(3\varphi_{\mathrm{ref}} - 2\varphi_{\mathrm{pu}} - \varphi_{\mathrm{pr}})\hbar}{\tau_{\mathrm{pr}}}, \qquad \text{(B3)}$$

which describes the tilt of the interference fringes in the phase maps in Sec. IV B 1. Here, we made use of the definition of $\varpi_{\mathrm{holo}}(k)$ and α_{opt} and neglected other constant phase terms.

b. Bound-state time evolution. In the next step we investigate the beating between the bound-state time evolution and the laser electric field which is affected by a frequency variation $\Delta\omega_{\mathrm{pu}}$ of the pump pulse. Since we are interested in a relative phase shift in a phase map, all parameters except for the frequency variation and the relative optical phases are assumed to be constant, and we neglect additional constant phase terms. The resulting expression

$$2\Delta\omega_{\mathrm{pu}}\tau_{\mathrm{pu}} = -\Delta\alpha_{\mathrm{opt}} \qquad \text{(B4)}$$

describes the relation between a phase shift in a phase map and the detuning of the pump frequency $\Delta\omega_{\mathrm{pu}}$. Hence, the relation

$$2\Delta\omega_{\mathrm{pu}}\tau_{\mathrm{pu}} = \Delta\varphi_{\mathrm{pr}} \qquad \text{(B5)}$$

describes the phase shift in a φ_{pr}-resolved phase map by using $\Delta\varphi_{\mathrm{ref}} = \Delta\varphi_{\mathrm{pu}} = 0$, as studied in Sec. IV B 2.

---

[1] M. Born, Zur Quantenmechanik der Stoßvorgänge, Z. Phys. **37**, 863 (1926).

[2] C. Cohen-Tannoudji, B. Diu, and F. Laloe, *Quantum Mechanics* (Wiley, New York, 1977), Vol. 1, pp. 3–889.

[3] A. T. J. B. Eppink and D. H. Parker, Velocity map imaging of ions and electrons using electrostatic lenses: Application in photoelectron and photofragment ion imaging of molecular oxygen, Rev. Sci. Instrum. **68**, 3477 (1997).

[4] R. Dörner, V. Mergel, O. Jagutzki, L. Spielberger, J. Ullrich, R. Moshammer, and H. Schmidt-Bocking, Cold target recoil ion momentum spectroscopy: A 'momentum microscope' to view atomic collision dynamics, Phys. Rep. **330**, 95 (2000).

[5] K. L. Reid, Photoelectron angular distribution, Annu. Rev. Phys. Chem. **54**, 397 (2003).

[6] C. F. de Morisson Faria and A. S. Maxwell, It is all about phases: Ultrafast holographic photoelectron imaging, Rep. Prog. Phys. **83**, 034401 (2020).

[7] E. Madelung, Quantentheorie in hydrodynamischer Form, Z. Phys. **40**, 322 (1927).

[8] K. Y. Bliokh, I. P. Ivanov, G. Guzzinati, L. Clark, R. Van Boxem, A. Béché, R. Juchtmans, M. A. Alonso, P. Schattschneider, F. Nori, and J. Verbeeck, Theory and applications of free-electron vortex states, Phys. Rep. **690**, 1 (2017).

[9] S. M. Lloyd, M. Babiker, G. Thirunavukkarasu, and J. Yuan, Electron vortices: Beams with orbital angular momentum, Rev. Mod. Phys. **89**, 035004 (2017).

[10] T. Bayer, C. Philipp, K. Eickhoff, and M. Wollenhaupt, Atomic photoionization dynamics in ultrashort cycloidal laser fields, Phy. Rev. A **102**, 013104 (2020).

[11] T. C. Weinacht, J. Ahn, and P. H. Bucksbaum, Controlling the shape of a quantum wavefunction, Nature (London) **397**, 233 (1999).

[12] J. Itatani, J. Levesque, D. Zeidler, H. Niikura, H. Pepin, J. C. Kieffer, P. B. Corkum, and D. M. Villeneuve, Tomographic imaging of molecular orbitals, Nature (London) **432**, 867 (2004).

[13] Y. Huismans, A. Rouzée, A. Gijsbertsen, J. H. Jungmann, A. S. Smolkowska, P. Logman, F. Lepine, C. Cauchy, S. Zamith, and T. Marchenko, Time-resolved holography with photoelectrons, Science **331**, 61 (2011).

[14] D. M. Villeneuve, P. Hockett, M. J. J. Vrakking, and H. Niikura, Coherent imaging of an attosecond electron wave packet, Science **356**, 1150 (2017).

[15] C. Warmuth, A. Tortschanoff, F. Milota, M. Shapiro, Y. Prior, I. S. Averbukh, W. Schleich, W. Jakubetz, and H. F. Kauffmann, Studying vibrational wavepacket dynamics by measuring fluorescence interference fluctuations, J. Chem. Phys. **112**, 5060 (2000).

[16] J. A. Cina, Wave-packet interferometry and molecular state reconstruction: Spectroscopic adventures on the left-hand side of the Schrödinger equation, Annu. Rev. Phys. Chem. **59**, 319 (2008).

[17] K. Ohmori, Wave-packet and coherent control dynamics, Annu. Rev. Phys. Chem. **60**, 487 (2009).

[18] A. Monmayrant, B. Chatel, and B. Girard, Quantum State Measurement using Coherent Transients, Phys. Rev. Lett. **96**, 103002 (2006).

[19] J. Mauritsson, T. Remetter, M. Swoboda, K. Klünder, A. L'Huillier, K. J. Schafer, O. Ghafur, F. Kelkensberg, W. Siu,

P. Johnsson, M. J. J. Vrakking, I. Znakovskaya, T. Uphues, S. Zherebtsov, M. F. Kling, F. Lepine, E. Benedetti, F. Ferrari, G. Sansone, and M. Nisoli, Attosecond Electron Spectroscopy Using a Novel Interferometric Pump-Probe Technique, Phys. Rev. Lett. **105**, 053001 (2010).

[20] K. Klünder, P. Johnsson, M. Swoboda, A. L'Huillier, G. Sansone, M. Nisoli, M. J. J. Vrakking, K. J. Schafer, and J. Mauritsson, Reconstruction of attosecond electron wave packets using quantum state holography, Phys. Rev. A **88**, 033404 (2013).

[21] K. Eickhoff, S. Kerbstadt, T. Bayer, and M. Wollenhaupt, Dynamic quantum state holography, Phys. Rev. A **101**, 013430 (2020).

[22] D. Pengel, S. Kerbstadt, D. Johannmeyer, L. Englert, T. Bayer, and M. Wollenhaupt, Electron Vortices in Femtosecond Multiphoton Ionization, Phys. Rev. Lett. **118**, 053003 (2017).

[23] T. Remetter, P. Johnsson, J. Mauritsson, K. Varju, Y. Ni, F. Lepine, E. Gustafsson, M. Kling, J. Khan, R. Lopez-Martens, K. J. Schafer, M. J. J. Vrakking, and A. L'Huillier, Attosecond electron wave packet interferometry, Nat. Phys. **2**, 323 (2006).

[24] X. B. Bian and A. D. Bandrauk, Attosecond Time-Resolved Imaging of Molecular Structure by Photoelectron Holography, Phys. Rev. Lett. **108**, 263003 (2012).

[25] D. Gábor, in *Nobel Lectures in Physics 1971–1980*, edited by S. Lundqvist (World Scientific, Singapore, 1992).

[26] D. Gábor, Holography, 1948-1971, Science **177**, 299 (1972).

[27] C. Leichtle, W. P. Schleich, I. S. Averbukh, and M. Shapiro, Quantum State Holography, Phys. Rev. Lett. **80**, 1418 (1998).

[28] I. S. Averbukh, M. Shapiro, C. Leichtle, and W. P. Schleich, Reconstructing wave packets by quantum-state holography, Phys. Rev. A **59**, 2163 (1999).

[29] T. Bayer, D. Gräfing, S. Kerbstadt, D. Pengel, K. Eickhoff, L. Englert, and M. Wollenhaupt, Time-resolved 3d imaging of ultrafast spin-orbit wave packet dynamics, New J. Phys. **21**, 033001 (2019).

[30] S. Kerbstadt, L. Gabrisch, K. Eickhoff, T. Bayer, and M. Wollenhaupt, Imaging multiple Rydberg wave packets from shaper-generated two-color femtosecond pump-probe sequences, Phys. Rev. A **99**, 013406 (2019).

[31] M. Wollenhaupt, M. Krug, J. Köhler, T. Bayer, C. Sarpe-Tudoran, and T. Baumert, Three-dimensional tomographic reconstruction of ultrashort free electron wave packets, Appl. Phys. B **95**, 647 (2009).

[32] K. Eickhoff, L. Feld, D. Köhnke, L. Englert, T. Bayer, and M. Wollenhaupt, Coherent control mechanisms in bichromatic multiphoton ionization, J. Phys. B **54**, 164002 (2021).

[33] S. Kerbstadt, D. Timmer, L. Englert, T. Bayer, and M. Wollenhaupt, Ultrashort polarization-tailored bichromatic fields from a CEP-stable white light supercontinuum, Opt. Express **25**, 12518 (2017).

[34] K. Eickhoff, L. Englert, T. Bayer, and M. Wollenhaupt, Multichromatic polarization-controlled pulse sequences for coherent control of multiphoton ionization, Front. Phys. **9**, 444 (2021).

[35] S. Kerbstadt, D. Pengel, D. Johannmeyer, L. Englert, T. Bayer, and M. Wollenhaupt, Control of photoelectron momentum distributions by bichromatic polarization-shaped laser fields, New J. Phys. **19**, 103017 (2017).

[36] J. C. Diels and W. Rudolph, *Ultrashort Laser Pulse Phenomena* (Academic, San Diego, 1996).

[37] S. Kerbstadt, K. Eickhoff, T. Bayer, and M. Wollenhaupt, Odd electron wave packets from cycloidal ultrashort laser fields, Nat. Commun. **10**, 658 (2019).

[38] A. Präkelt, M. Wollenhaupt, C. Sarpe-Tudoran, and T. Baumert, Phase control of a two-photon transition with shaped femtosecond laser-pulse sequences, Phys. Rev. A **70**, 063407 (2004).

[39] A. W. Albrecht, J. D. Hybl, S. M. Gallagher Faeder, and D. M. Jonas, Experimental distinction between phase shifts and time delays: Implications for femtosecond spectroscopy and coherent control of chemical reactions, J. Chem. Phys. **111**, 10934 (1999).

[40] M. Wollenhaupt, A. Assion, D. Liese, C. Sarpe-Tudoran, T. Baumert, S. Zamith, M. A. Bouchene, B. Girard, A. Flettner, U. Weichmann, and G. Gerber, Interferences of Ultrashort Free Electron Wave Packets, Phys. Rev. Lett. **89**, 173001 (2002).

[41] N. Dudovich, B. Dayan, S. M. Gallagher Faeder, and Y. Silberberg, Transform-Limited Pulses are not Optimal for Resonant Multiphoton Transitions, Phys. Rev. Lett. **86**, 47 (2001).

[42] B. J. Sussman, Five ways to the nonresonant dynamic Stark effect, Am. J. Phys. **79**, 477 (2011).

[43] A. Wituschek, J. von Vangerow, J. Grzesiak, F. Stienkemeier, and M. Mudrich, A simple photoionization scheme for characterizing electron and ion spectrometers, Rev. Sci. Instrum. **87**, 083105 (2016).

[44] T. Brixner and G. Gerber, Femtosecond polarization pulse shaping, Opt. Lett. **26**, 557 (2001).

[45] A. M. Weiner, Ultrafast optical pulse shaping: A tutorial review, Opt. Commun. **284**, 3669 (2011).

[46] S. Kerbstadt, L. Englert, T. Bayer, and M. Wollenhaupt, Ultrashort polarization-tailored bichromatic fields, J. Mod. Opt. **64**, 1010 (2017).

[47] A. Präkelt, M. Wollenhaupt, A. Assion, C. Horn, C. Sarpe-Tudoran, M. Winter, and T. Baumert, Compact, robust and flexible setup for femtosecond pulse shaping, Rev. Sci. Instrum. **74**, 4950 (2003).

[48] A. Kramida, Y. Rachenko, and J. Reader, NIST atomic spectra database, NIST (2018). The online database is available at https://www.nist.gov/pml/atomic-spectra-database.

[49] J. Köhler, M. Wollenhaupt, T. Bayer, C. Sarpe, and T. Baumert, Zeptosecond precision pulse shaping, Opt. Express **19**, 11638 (2011).

[50] A. C. Kak and M. Slaney, *Principles of Computerized Tomographic Imaging* (IEEE Press, New York, 1988).

[51] S. Kerbstadt, K. Eickhoff, T. Bayer, and M. Wollenhaupt, Control of free electron wave packets by polarization-tailored ultrashort bichromatic laser fields, Adv. Phys.: X **4**, 1672583 (2019).

[52] T. Baumert, T. Brixner, V. Seyfried, M. Strehle, and G. Gerber, Femtosecond pulse shaping by an evolutionary algorithm with feedback, Appl. Phys. B **65**, 779 (1997).

[53] D. Yelin, D. Meshulach, and Y. Silberberg, Adaptive femtosecond pulse compression, Opt. Lett. **22**, 1793 (1997).

[54] A. M. Weiner, Femtosecond pulse shaping using spatial light modulators, Rev. Sci. Instrum. **71**, 1929 (2000).

[55] D. Meshulach and Y. Silberberg, Coherent quantum control of two-photon transitions by a femtosecond laser pulse, Nature (London) **396**, 239 (1998).

[56] M. Wollenhaupt, A. Präkelt, C. Sarpe-Tudoran, D. Liese, T. Bayer, and T. Baumert, Femtosecond strong-field quantum

control with sinusoidally phase-modulated pulses, Phys. Rev. A **73**, 063409 (2006).

[57] D. Pengel, S. Kerbstadt, L. Englert, T. Bayer, and M. Wollenhaupt, Control of three-dimensional electron vortices from femtosecond multiphoton ionization, Phys. Rev. A **96**, 043426 (2017).

[58] S. Mukamel, Multidimensional femtosecond correlation spectroscopies of electronic and vibrational excitations, Annu. Rev. Phys. Chem. **51**, 691 (2000).

[59] D. M. Jonas, Two-dimensional femtosecond spectroscopy, Annu. Rev. Phys. Chem. **54**, 425 (2003).

[60] B. Kaufman, T. Rozgonyi, P. Marquetand, and T. Weinacht, Coherent Control of Internal Conversion in Strong-Field Molecular Ionization, Phys. Rev. Lett. **125**, 053202 (2020).

[61] T. Brixner, G. Krampert, T. Pfeifer, R. Selle, G. Gerber, M. Wollenhaupt, O. Graefe, C. Horn, D. Liese, and T. Baumert, Quantum Control by Ultrafast Polarization Shaping, Phys. Rev. Lett. **92**, 208301 (2004).

[62] C. Hofmann, A. S. Landsman, and U. Keller, Attoclock revisited on electron tunnelling time, J. Mod. Opt. **66**, 1052 (2019).

[63] W. Domcke and D. R. Yarkony, Role of conical intersections in molecular spectroscopy and photoinduced chemical dynamics, Annu. Rev. Phys. Chem. **63**, 325 (2012).

[64] T. Bayer, M. Wollenhaupt, H. Braun, and T. Baumert, Ultrafast and efficient control of coherent electron dynamics via SPODS, Adv. Chem. Phys. **159**, 235 (2016).

[65] J. I. Steinfeld, *Molecules and Radiation: An Introduction to Modern Molecular Spectroscopy* (MIT Press, Cambridge, 1985).

[66] D. Meshulach and Y. Silberberg, Coherent quantum control of multiphoton transitions by shaped ultrashort optical pulses, Phys. Rev. A **60**, 1287 (1999).

[67] A. Gandman, L. Chuntonov, L. Rybak, and Z. Amitay, Coherent phase control of resonance-mediated (2+1) three-photon absorption, Phys. Rev. A **75**, 031401(R) (2007).